Journal of Materials Chemistry C

Reducing dielectric loss and enhancing electrical insulation for multilayer polymer films by nanoconfined ion transport under high poling electric fields

Journal:	*Journal of Materials Chemistry C*
Manuscript ID	TC-ART-01-2020-000522.R1
Article Type:	Paper
Date Submitted by the Author:	25-Feb-2020

Complete List of Authors:	Chen, Xinyue; Case Western Reserve University, Macromolecular Science and Engineering Allahyarov, Elshad; Heinrich-Heine-Universitat Dusseldorf, Insitut fur Theoretische Physik II; Joint Institute for High Temperatures, Russian Academy of Sciences , Theoretical Department Langhe, Deepak; PolymerPlus, LLC Ponting, Michael; PolymerPlus, LLC Li, Ruipeng; Brookhaven National Laboratory Fukuto, Masafumi; Brookhaven National Laboratory, Condensed Matter Physics and Materials Science Department Schuele, Donald; Case Western Reserve University, Macromolecular Science and Engineering Baer, Eric; Case Western Reserve University, Zhu, Lei; Case Western Reserve University, Macromolecular Science and Engineering

Reducing dielectric loss and enhancing electrical insulation for multilayer polymer films by nanoconfined ion transport under high poling electric fields

Xinyue Chen,[a] Elshad Allahyarov,[a,b,c,*] Deepak Langhe,[d] Michael Ponting,[d] Ruipeng Li,[e] Masafumi Fukuto,[e] Donald E. Schuele,[f] Eric Baer,[a] and Lei Zhu[a,*]

[a] *Center for Layered Polymeric Systems (CLiPS) and Department of Macromolecular Science and Engineering, Case Western Reserve University, Cleveland, Ohio 44106-7202, United States*

[b] *Theoretische Chemie, Universität Duisburg-Essen, D-45141 Essen, Germany*

[c] *Theoretical Department, Joint Institute for High Temperatures, Russian Academy of Sciences, 13/19 Izhorskaya street, Moscow 125412, Russia*

[d] *PolymerPlus, LLC, 7700 Hub Pkwy, Valley View, Ohio 44125, United States*

[e] *National Synchrotron Light Source II, Brookhaven National Laboratory, Upton, New York 11973, United States*

[f] *Department of Physics, Case Western Reserve University, Cleveland, Ohio 44106, United States*

* Corresponding authors. Email addresses: lxz121@case.edu (L. Zhu), exa54@case.edu (E. Allahyarov)

Abstract

High temperature polar polymers have demonstrated a potential for good thermal stability and high dielectric constant at the same time. However, polarization of contaminated impurity ions in polar polymers, even at the ppm level, can significantly increase the dielectric loss at high temperature and low frequencies. One effective strategy to mitigate this problem is to multilayer them with a high temperature nonpolar dielectric polymer to confine impurity ion transport at the nanometer scale. In this study, confined ion transport in high temperature polycarbonate (HTPC)/poly(vinylidene fluoride) (PVDF) multilayer films under high AC electric fields was studied using a direct analytical simulation method. Different from the ion transport under low fields, the ion diffusion model failed to describe the ion transport under high electric fields. An exponential ion distribution profile, which was observed for the DC poling situation, was employed to implement the direct analytical simulation. Confined impurity ion transport under high AC fields was quantitatively understood. As the AC field increased, the mobile ion concentration decreased whereas the diffusion coefficient increased. The decrease of mobile ion concentration was explained by the blockage of impurity ions by the HTPC layers. This knowledge helped the determination of optimal conditions to polarize impurity ions from the PVDF layers into the HTPC layers. After cooling below the glass transition temperature of HTPC, polarized impurity ions were locked inside the HTPC layers. As a result, increased discharge efficiency and enhanced electrical insulation (i.e., increased dielectric breakdown strength) were achieved for the polarized multilayer films.

Keywords: Multilayer films, ion transport, polycarbonate, poly(vinylidene fluoride), dielectric insulation

Introduction

Polymer film capacitors play an important role in the power electronic system of electric vehicles.[1-3] Different from polymer-based supercapacitors,[4] which store the electric energy in the electric double layer (EDL),[5] polymer film capacitors store electric energy in the polarized dipoles.[6] Current state-of-the-art DC-link capacitors utilize biaxially oriented polypropylene (BOPP) films with a thickness as thin as 2.5 μm without sacrificing the excellent dielectric performance. Nonetheless, the temperature rating of typical BOPP film capacitors is only 85 °C (above which the lifetime significantly decreases),[7, 8] much lower than the ambient temperature (140 °C) in a power electronic unit. As a compromise, a 60-70 °C water-cooling system is needed to maintain the capacitor temperature not to exceed 85 °C. This adds an additional cost to electric vehicles. It is therefore desired to develop high temperature capacitor films with a similar or even lower cost as BOPP.[6, 9-11] Because of the low price of isotactic PP, high dielectric constant polymers should also be pursued for direct miniaturization to achieve this goal.

One approach to simultaneously achieve high thermal stability and high dielectric constant is to utilize high temperature polar polymers such as aromatic polythiourea.[12-15] However, these polar polymers are easily contaminated with impurity ions (even at ppm level) and ionic conduction can significantly increase the dielectric loss, especially at high temperatures and low frequencies.[16, 17] An effective approach to mitigate this problem is to multilayer these polar polymers with a nonpolar linear dielectric polymer.[18-21] In this way, the ionic transport in the polar polymer can be confined at the nanometer scale to reduce impurity ion conduction loss.[22] Meanwhile, the nonpolar polymer can also encapsulate the polar polymer to prevent absorbing moisture from the ambient environment.

In the past decade, we have developed polycarbonate (PC)/poly(vinylidene fluoride)

(PVDF) multilayer films (MLFs).[23] By utilizing the high glass transition temperature (T_g) PC (HTPC), whose T_g is about 165 °C, HTPC/PVDF MLFs can exhibit both good thermal stability and high dielectric constant at the same time. However, the dielectric loss for these MLFs (e.g., the dissipation factor, tanδ, ~0.005 at 1 kHz at room temperature) is still significantly higher than that of BOPP (tanδ ~0.0003).[24] One important loss mechanism is the impurity ion conduction in the PVDF layer under an applied electric field.[16, 22] In a recent study, we quantified the nanoconfinement effect for impurity ions in PVDF by using a direct analytical simulation method.[25] Compared to the reported Sawada analysis of the broadband dielectric spectroscopy (BDS) data for extracted single-layer PVDF,[16] this direct analytical simulation is more accurate. However, when the applied AC electric field increased to above 4 MV/m, the direct analytical simulation using the ion diffusion model failed. Note that the applied electric field for polymer film capacitors is often 100-200 MV/m in practical applications such as electric vehicles. Therefore, understanding impurity ion transport under high electric fields is very relevant to practical applications.

In this study, we utilized the exponential ion distribution function, which is often observed under a DC poling process,[5] to implement the direct analytical simulation. The high-field impurity ion transport can be successfully simulated. The obtained knowledge helps the determination of the optimal electric poling conditions to drive impurity ions from the PVDF layers into the neighboring HTPC layers.[26] By cooling far below the T_g of HTPC, these locked interfacial space charges are demonstrated to increase the discharge efficiency, reduce leakage current, and improve dielectric breakdown strength.

Experimental

Materials

HTPC (Apec® 1745) resin was purchased from Covestro (Pittsburgh, PA). PVDF (Solef® 6010) and polysulfone (PSF, Udel® P-3703) resins were purchased from Solvay Plastics (Alpharetta, GA). All resins were dried under vacuum for two days prior to the multilayer coextrusion.

MLF preparation and high temperature polarization to lock impurity ions in HTPC layers

The multilayer coextrusion was performed at 280 °C with two single-screw extruders at PolymerPlus, LLC.[19] The coextrusion temperature was determined by the rheological compatibility of the HTPC and PVDF, which was measured using a melt flow indexer (MFI), Kayeness Galaxy1, at a shear rate similar to the extrusion condition (10 s^{-1}, see Figure S1 in the Supporting Information). The melt coextrusion process was described in detail in previous publications.[27] Briefly, during coextrusion of HTPC/PVDF 50/50 (vol./vol.) 33-layer (33L) film, polymer melts were firstly converged by a three-layer ABA (HTPC/PVDF/HTPC) feedblock with a volume ratio of 25/50/25. Then, the ABA trilayer went through four multilayers, where the polymer melts were split, spread, and restacked together. Finally, MLFs were laminated with two low-density polyethylene (LDPE) skin layers on both surfaces before exiting the die (20 inch wide with a 500 μm slit opening). The thickness of MLFs was around 12 μm, which was controlled by the take-off speed using a chill roll. The LDPE skin layers were removed and MLFs were dried thoroughly in a vacuum oven for 24 h before later dielectric characterization. The coextrusion detail of the PSF/PVDF 50/50 (vol./vol.) was reported previously.[26, 28] HTPC or PSF control film was prepared by using the same coextrusion process as the MLFs with both A and B being the same polymer.

The polarization process of impurity ions from the PVDF layers to the HTPC layers was carried out as the following. After drying at 50 °C for 24 h, the MLF sample was sandwiched between two conductive silicone rubber sheets (0.7 mm thick with a conductivity of ca. 0.03 S/cm) and two 4-cm diameter gold-plated copper discs to avoid any mechanical damage and dielectric breakdown during electric poling at high temperatures. Electric poling was then performed at 150 °C, which was 15 °C below the T_g (165 °C) of HTPC, for a predetermined amount of time to drive the impurity ions from the PVDF layers into the HTPC layers. Various combinations of DC and AC voltages were applied to compare the poling effect. While maintaining the poling electric field, the sample was cooled to room temperature. After coating with metal electrodes, the polarized sample was ready for the other dielectric characterizations.

Instruments and characterization methods

D-E loops were measured using a Radiant Technology Premiere II ferroelectric tester at a frequency of 10 Hz using a sinusoidal wave function. Aluminum (Al) electrodes (10 nm thick) were evaporated on both sides of the film with a diameter of 3.2 mm. Samples were immersed in a silicone oil bath to avoid corona discharge in air. High-temperature tests were performed using a temperature-controlled heating stage, Arex-6 Conn. Pro System (Chemglass). Novocontrol high-voltage broadband dielectric spectroscopy (HV-BDS), equipped with a high-voltage interface HVB4000, was used to study the impurity ion transport and to polarize the impurity ions in PVDF layers as well. The HVB4000 interface could provide ±2000 V (peak-to-peak) high voltage with frequency up to 10^4 Hz. The film samples were coated with ~50 nm Al electrodes on both sides using a Denton Vacuum BenchTop Turbo thermal evaporator (Moorestown, NJ). The electrode diameter was 1.0 cm (area 0.785 cm^2). Frequency-scan real

and imaginary relative permittivities (ε_r' and ε_r'') in the range of 10^{-2}-10^4 Hz were measured at 130 °C (note, this temperature was chosen because the fast-ion conduction peak was well separated from other relaxation peaks). To study the in-situ electric poling effect, a dried MLF sample was heated at a heating rate of 5 °C/min from 100 °C to the poling temperature (150 °C), where a unipolar (DC+AC at 1 Hz) electric field was applied for 2 h to drive the impurity ions from the PVDF layers into the HTPC layers. While holding the poling electric field, the sample was cooled to 100 °C to avoid the relaxation or recombination of impurity ions. To quantitatively evaluate the poling efficiency, HV-BDS (2.10 MV/m DC + 2.10 MV/m AC) frequency-scans in the range of 10^{-2}~10^4 Hz at 100 °C were measured before and immediately after electric poling. Meanwhile, HV-BDS frequency-scans were also measured after annealing at 100 °C for 1 and 6 h to detect if impurity ions could relax back into the PVDF layers. Finally, HV-BDS frequency-scans at different temperatures from 20 to 150 °C were carried out to test the thermal stability of HTPC-locked impurity ions.

A Keithley 6517B electrometer was used to measure the leakage current, and Novocontrol Concept 80 was used to control the temperature. Film samples were coated with ca. 50 nm Al electrodes on both sides with a diameter of 10.0 mm. When a constant electric field was applied across the sample, the leakage current was recorded for 1 h at different temperatures.[29] At each temperature, a fresh sample was tested from low to high electric fields. The bulk conductivity (σ) was calculated from the current density (J) and the electric field (E): $\sigma = J/E$.

A Quadtech Guardian 20kV HiPot tester was used to test the breakdown strength of MLFs. Film samples were placed between the electrodes on a home-made fixture with the ramping voltage of 500 V/s until electrical breakdown. Both sides of the film were coated with ca. 50 nm Al electrodes (diameter 3.2 mm).

Two-dimensional (2D) small-angle X-ray scattering (SAXS) and wide-angle X-ray diffraction (WAXD) patterns were collected at the 11-BM Complex Materials Scattering (CMS) beamline of the National Synchrotron Light Source II (NSLS-II), Brookhaven National Laboratory. The monochromatized X-ray wavelength was $\lambda = 0.0918$ nm. A Pilatus 2M (Dectris) detector was used for SAXS and an in-vacuum CCD (Photonic Science) detector was used for WAXD experiments. To allow the SAXS signal to pass through, the WAXD detector was shifted and tilted by ~71° from the incident X-ray beam direction. The distances between the sample and detectors were 0.235 m for WAXD and 2.99 m for SAXS, which were calibrated using silver behenate with the first-order reflection at a scattering vector of $q = 4\pi\sin\theta/\lambda = 1.076$ nm^{-1} (θ is the half scattering angle). The data acquisition time for each pattern was 10 s. Fit2D was used for data analysis.

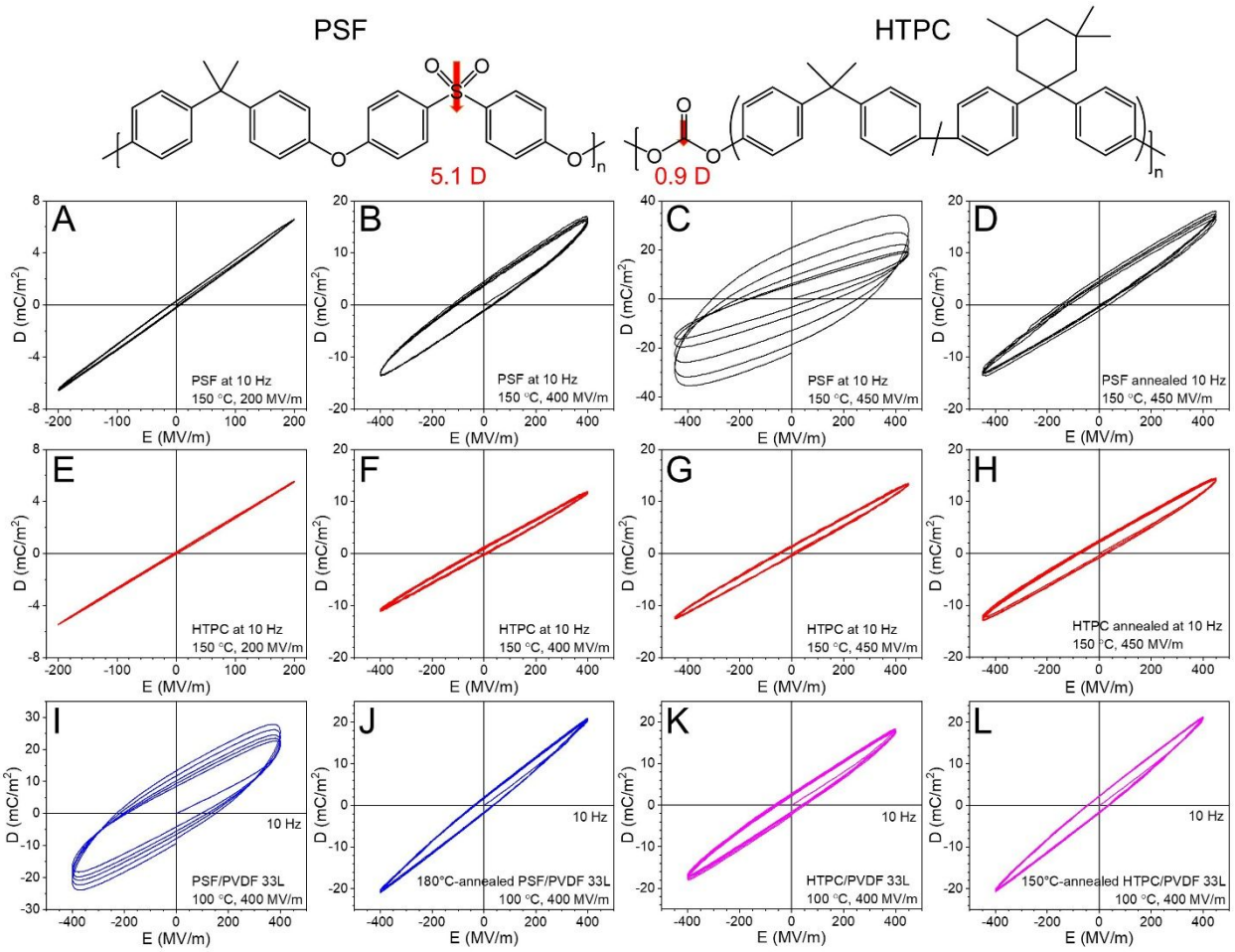

Figure 1. Bipolar D-E loops for the as-extruded PSF control film at (A) 200, (B) 400, (C) 450 MV/m, and (D) the 180 °C-annealed PSF film at 450 MV/m. Bipolar D-E loops for the as-extruded HTPC film at (E) 200, (F) 400, (G) 450 MV/m, and (H) the 150 °C-annealed HTPC film at 450 MV/m. The test temperature for both control films was 150 °C. Bipolar D-E loops for the PSF/PVDF 50/50 33L (I) as-extruded and (J) 180 °C-annealed films, and the HTPC/PVDF 50/50 33L (K) as-extruded and (L) 150 °C-annealed films at 400 MV/m. The test temperature for both MLFs was 100 °C. For all tests, the poling frequency was 10 Hz with a sinusoidal waveform. The top panel shows the chemical structures of PSF and HTPC, together with estimated dipole moments of the sulfone and carbonate groups in the polymer chains.

Results and discussion

Ferroelectric switching of polar amorphous PSF at high poling fields and high temperatures

In a previous study,[26] we achieved the reduction of impurity ion conduction in PSF/PVDF MLFs by electric poling at 165 °C, which was 20 °C lower than the T_g (185 °C) of PSF. As we know, both HTPC and PSF have relatively high T_gs, which is critical to keep high insulation at high

temperatures.[30] However, it was found that PSF and HTPC behaved quite differently at high poling electric fields and high temperatures. Figures 1A-C and 1E-G compare the D-E loop behaviors for the as-extruded PSF and the HTPC control films at 150 °C, respectively. When the poling field was below 400 MV/m, the as-extruded PSF control film exhibited broader D-E loops than the as-extruded HTPC control film; however, all loops still appeared more or less linear and slim. When the poling field increased to 450 MV/m, significant hysteresis gradually developed during continuous bipolar poling for the as-extruded PSF control film, whereas the as-extruded HTPC control film still exhibited narrow linear loops. Recently, we reported ferroelectric switching for amorphous nylons, and the ferroelectricity was attributed to the electric field-induced segmental motion, which was similar to the cooperative segmental motion during glass transition.[31] Therefore, the significant hysteresis in Figure 1C could be attributed to the high electric field-induced ferroelectric switching of polar amorphous PSF, even though the temperature was below its T_g. The top panel of Figure 1 shows the chemical structures of PSF and HTPC, together with the estimated chain conformations and dipole moment. If both PSF and HTPC adopted the *trans* configuration for the sulfonyl and carbonate groups, their dipole moments were 5.1 D [32] and 0.9 D,[33, 34] respectively. Obviously, PSF is much more polar than HTPC in the bulk, and it is likely to show certain ferroelectricity if the free volume is high. After thermal annealing at 180 °C for 10 min, the hysteresis loops became much narrower (Figure 1D), indicating the suppression of ferroelectric switching. It is well-known that physical aging could reduce free volume for glassy polymers.[35, 36] We consider that the tighter packing of amorphous PSF chains after physical aging suppressed ferroelectric switching in the glassy phase. A similar observation was also reported for the amorphous nylon, Selar.[31] Careful inspection of the D-E loops for PSF and HTPC control films in Figure 1, the linear D-E loops appeared to be asymmetric with respect

to the origin of the plots. This was attributed to the existence of electronic (or resistive) conduction and/or small remnant polarization during bipolar poling of the samples.[17]

From the above result, as-extruded HTPC/PVDF MLFs should be more advantageous than as-extruded PSF/PVDF MLFs for high-temperature capacitor applications. This is reflected by comparing the bipolar D-E loops for as-extruded PSF/PVDF and HTPC/PVDF 50/50 33L films in Figures 1I and K, respectively. Clearly, the much broader hysteresis loops for the as-extruded PSF/PVDF 33L film in Figure 1I than those for the as-extruded HTPC/PVDF 33L film in Figure 1K were attributed to the high electric field-induced ferroelectric switching of polar PSF. After physical aging of the PSF/PVDF 33L film at 180 °C for 10 min, the D-E loops became slimmer because of the reduced free volume in PSF (Figure 1J). Meanwhile, after physical aging of the HTPC/PVDF 33L film at 150 °C for 2 h, the D-E loops also became slightly slimmer (Figure 1L). This could be attributed to the increased crystallinity and perfection of PVDF crystals, as we reported recently.[28] For PVDF-based MLFs, poor secondary PVDF crystals could also contribute to the ferroelectric switching during bipolar poling. Thermal annealing at high temperatures eliminated poor PVDF crystals and thus reduced ferroelectric switching. In the following study, we will focus on HTPC/PVDF rather than PSF/PVDF MLFs.

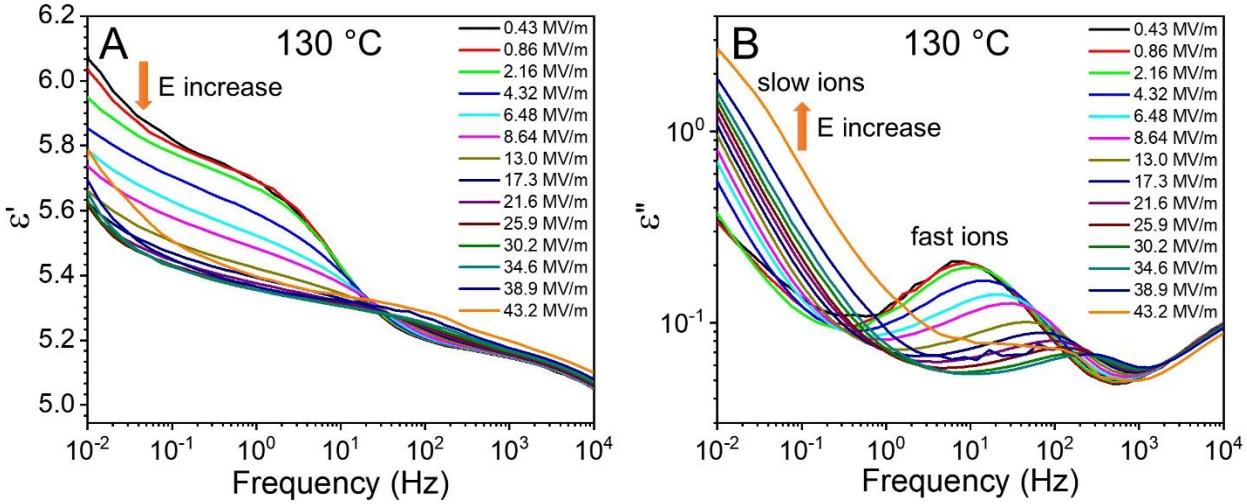

Figure 2. Frequency-scan HV-BDS results of (A) ε′ and (B) ε″ under different AC electric fields at 130 °C. The average film thickness was 11.6 μm.

Confined ion transport under high electric fields in HTPC/PVDF multilayer films

From the BDS results in Figure 2, the fast-ion conduction peak around 10^{-1} - 10^{2} Hz had some overlap with the α_c relaxation at higher frequencies and the slow-ion conduction peak at lower frequencies. To accurately determine fast-ion concentration (n_0) and diffusion coefficient (D_0), the contribution from the fast-ion conduction for ε' and ε'' should be deconvoluted firstly. For this purpose, we utilized a multimode Havriliak-Negami (HN) formula, which is a combination of Cole-Cole and Cole-Davidson relaxations:[37]

$$\varepsilon_{HN}(\omega) = \varepsilon_\infty + \sum_{j=1}^{3} \frac{\varepsilon_s - \varepsilon_\infty}{\left(1 + (i\omega\tau_j)^{1-\alpha_j}\right)^{\beta_j}} \quad (1)$$

Here, $\tau_j = 1/\omega_j$ corresponds to the loss peak in $\varepsilon''_{HN}(\omega)$ and denotes characteristic relaxation times of the medium: τ_1 is the dipolar relaxation time (or the reorientation time of dipoles), τ_2 is the ionic relaxation time, and τ_3 is the electronic relaxation time. At the corresponding frequency, ω_j, the dielectric function $\varepsilon''_{HN}(\omega)$ exhibits a peak. In Eqn. (1), ε_∞ is the permittivity at the high-frequency limit, ε_s is the low-frequency permittivity, and the exponents, α_j and β_j, describe the asymmetry and broadness of the corresponding spectrum. For $\beta_j = 1$, the HN equation reduces

to the Cole-Cole equation. For $\alpha_j = 1$, it reduces to the Cole-Davidson equation. The exponential coefficients in the HN equation obey the following condition: $0 < \alpha_j \leq 1$ and $0 < \alpha_j\beta_j \leq 1$.

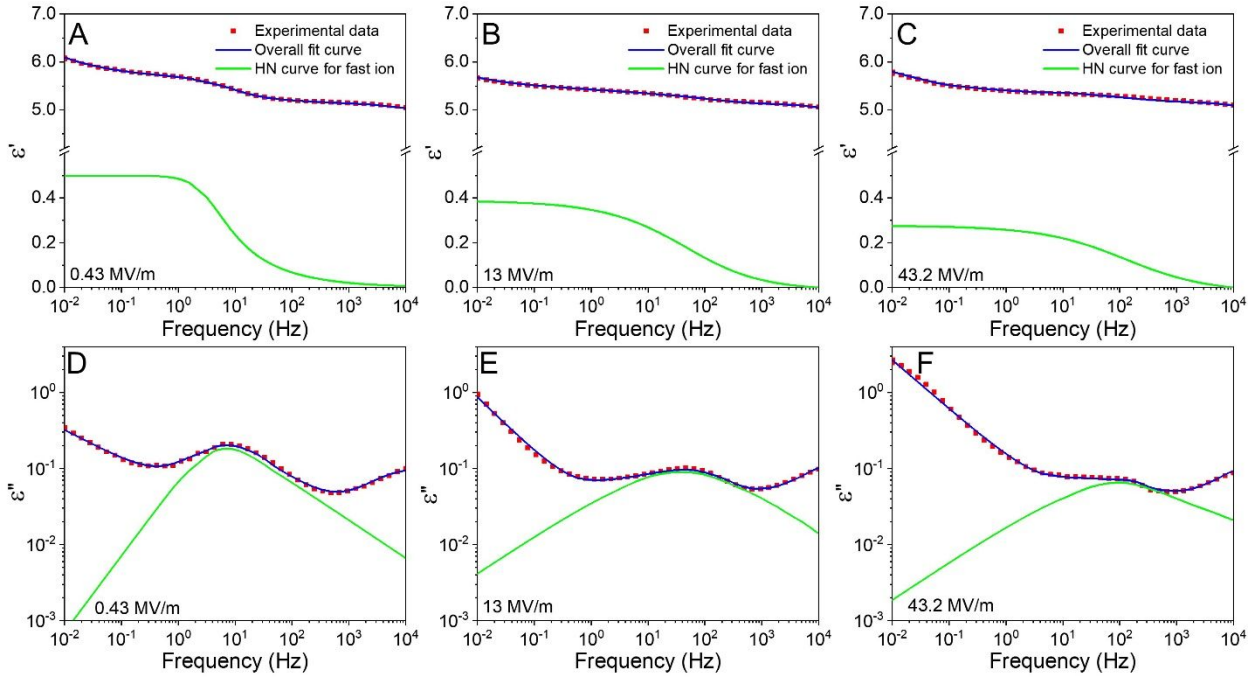

Figure 3. HN-deconvoluted (A-C) ε' and (D-F) ε'' curves for fast ions in the HTPC/PVDF 33L film (11.6 μm thick) for the applied field at (A,D) 0.43 MV/m, (B,E) 13 MV/m, and (C,F) 43.2 MV/m, respectively. Solid symbols: experimental data, blue curves: overall fit curves, and green curves: HN curves for fast ions. HN-fit curves for the $\alpha_{c,PVDF}$ relaxation and slow-ion conduction are not shown for clarity. Measurements were performed at 130 °C.

Deconvolution of the experimental ε' and ε'' spectra under different electric fields (0.43-43.2 MV/m) at 130 °C using the HN theory are shown in Figure 3 and Figure S2. The overall fit curves matched well with the experimental data. The deconvoluted ε' and ε'' curves were obtained and then used for the subsequent analytical simulation to extract n_0 and D_0 for fast ions in PVDF as a function of temperature. Detailed simulation procedure is described below.

Analytical simulation of confined ion transport under high electric fields

Under high AC electric fields, traditional analytical simulation using the linear perturbation theory[38, 39] fails, because of significant polarization of the ionic species at the blocking electrode boundaries. Here, two different approaches can be used to calculate the ionic polarization, $P_{ion}(\omega)$, as a function of frequency. The first approach, referred hereafter as approach I, is based on the modified linear perturbation theory. This is applicable only at low to medium electric fields (e.g., up to 6 MV/m). The second approach, hereafter referred to as approach II, is a completely new theory devised to investigate ionic polarization under high electric fields (e.g., > 6 MV/m). It is expected that in the limit of weak fields, approach II reproduces the results of approach I. Scheme 1 shows a single-layer film and an ABA trilayer film containing mobile ions under an external voltage $-|V_0|$.

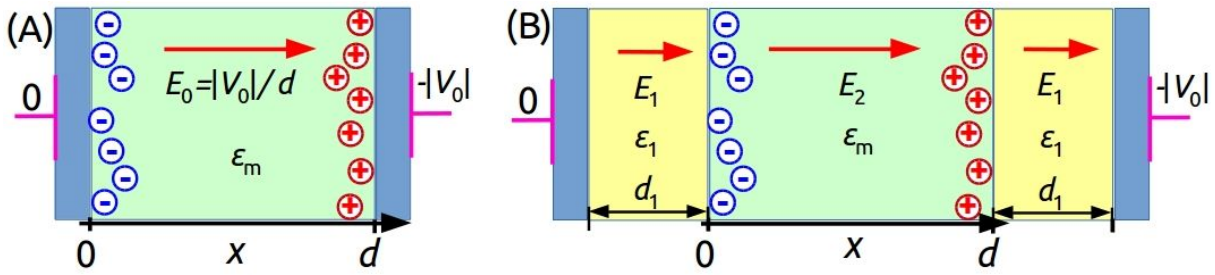

Scheme 1. Schematics of the simulation systems: (A) a single PVDF layer (green) and (B) a HTCP/PVDF/HTCP trilayer film with the middle PVDF layer containing mobile ions (assuming single valence). The PVDF layer has a thickness of d and a dielectric permittivity ε_m. The HTCP layers (yellow) have a thickness of d_1 and a permittivity ε_1. The metal electrodes are colored in blue. The macroscopic electric field in the single PVDF layer is denoted as E_0, and in the middle PVDF layer of the trilayer film is denoted as E_2. The field in the HTPC layer is denoted as E_1. The applied voltage is $-|V_0|$.

Approach I. A full description of the linear perturbation theory for the calculation of $P_{ion}(\omega)$ under low fields has been outlined in our recent report.[25] Ionic profiles in this linear

approach are defined as (see the Supporting Information in ref. 25),

$$n_+(x,\omega) = n_0 + \eta_+(x,\omega)e^{i\omega t} \quad (2)$$

$$n_-(x,\omega) = n_0 + \eta_-(x,\omega)e^{i\omega t} \quad (3)$$

where n_0 is the bulk ion concentration, η_+ and η_- are the perturbative parts of the ionic concentration. In the framework of the linear theory, these perturbations are defined as,

$$\frac{\eta_+(x,\omega)}{n_0} = -A_0\frac{\sinh(B(x-d/2))}{\sinh(Bd/2)+i\frac{\omega\lambda^2}{D_0}\cosh(Bd/2)Bd/2} \quad (4)$$

$$\frac{\eta_-(x,\omega))}{n_0} = A_0\frac{\sinh(B(x-d/2))}{\sinh(Bd/2)+i\frac{\omega\lambda^2}{D_0}\cosh(Bd/2)Bd/2} \quad (5)$$

and are smaller than the n_0. In Eqns. (2-5), $\lambda(\omega) = \sqrt{(\varepsilon_m + \epsilon(\omega))\,\varepsilon_0 k_B T/\left(2n_o q^2\right)}$ is the Debye screening length, $A_0 = \frac{qV_0(B\lambda)^2}{2k_B T}$ is a dimensionless parameter, $B(\omega) = \sqrt{1/\lambda^2(\omega) + i\omega/D_0}$ is a parameter with a unit of reciprocal length, ω is angular frequency ($\omega = 2\pi f$, where f is frequency in Hz), and the distance x is measured from the left wall of the PVDF single layer (Scheme 1A). Both parameters, A_0 and B, are complex functions of n_0, D_0, and ω. The density perturbations η_+ and η_- are odd functions around the mid-plane point $x = d/2$ (d is the PVDF layer thickness), meaning that if they are positive at one of the film boundaries, they are negative at the other film boundary.

We assume that a modified version of the perturbative profiles given by Eqns. (4-5) can be used for the ions under high poling fields. For the negative voltage $V_0 = -|V_0| < 0$ (i.e., the positive ions screen the right plane and the negative ions screen the left plane; see Scheme 1), we rewrite Eqns. (4-5) as,

$$\frac{\eta_+(x,\omega)}{n_0} = -CA_0\frac{\sinh(Bx)}{\sinh(Bd)+i\omega\lambda^2 Bd\cosh(Bd)/D_0} \quad (6)$$

$$\frac{\eta_-(x,\omega)}{n_0} = CA_0\frac{\sinh(B(x-d))}{\sinh(Bd)+i\omega\lambda^2 Bd\cosh(Bd)/D_0} \tag{7}$$

where the distance x changes from 0 to d, and the ionic profiles are hyperbolic functions without the oddness feature. The constant C is introduced to normalize the ionic profiles η_+ and η_- to the bulk ionic density n_0 for each type of ions,

$$\frac{1}{d}\mathrm{Re}\left(\int_0^d \eta_+(x)dx\right) = n_0 \tag{8}$$

$$\frac{1}{d}\mathrm{Re}\left(\int_0^d \eta_-(x)dx\right) = n_0 \tag{9}$$

Integration of $\eta_+(x)$ [or $\eta_-(x)$] gives,

$$\int_0^d \eta_+(x)dx = -\frac{CA_0n_0}{B}\frac{\cosh(Bd)-1}{\sinh(Bd)+i\omega\lambda^2 Bd\cosh(Bd)/D_0} \tag{10}$$

Thus, the constant C, which is positive, is derived as,

$$C = \left|\mathrm{Re}\left(\frac{Bd}{A_0}\frac{\sinh(Bd)+i\omega\lambda^2 Bd\cosh(Bd)/D_0}{\cosh(Bd)-1}\right)\right| \tag{11}$$

The charge density, defined as,

$$\rho_i(x,\omega) = q\eta_+(x,\omega) - q\eta_-(x,\omega) \tag{12}$$

now becomes,

$$\rho_i(x,\omega) = -2qCA_0n_0\frac{\cosh(Bd)\sinh\left(Bx-Bd\right)}{\sinh(Bd)+i\omega\lambda^2 Bd\cosh(Bd)/D_0} \tag{13}$$

As a consequence, for the polarization of the impurity ions in the PVDF layer, $P_{ion}(\omega)$, defined as

$$P_{ion}(\omega) = \frac{1}{d}\int_0^d x\rho_i(x,\omega)dx \tag{14}$$

we get,

$$P_{ion}(\omega) = C\cosh(Bd)\frac{\epsilon_0\epsilon_m V_0}{d}\frac{\sinh(Bd)-Bd\cosh(Bd)}{\sinh(Bd)+i\omega\lambda^2 Bd\cosh(Bd)/D_0} \tag{15}$$

This is the final expression for the ionic polarization of a single PVDF layer of a thickness *d* placed under the negative voltage -$|V_0|$ (see Scheme 1A).

Approach II. When the applied field is high, approach I also fails, and we now construct the following ionic profiles,[5, 40]

$$n_+(x,\omega) = \eta_+(x)e^{i\omega t} \tag{16}$$

$$n_-(x,\omega) = \eta_-(x)e^{i\omega t} \tag{17}$$

Here, we assume that under strong fields and in the AC steady state, the ions oscillate at the same frequency as the applied electric field. With these profiles, the Nernst-Planck equations for the ionic current densities j_+ and j_- (for details see ref. 25) are modified to,

$$j_+(x)e^{i\omega t} = -D_0\frac{\partial\eta_+}{\partial x}e^{i\omega t}+\mu\eta_+(x)E_\ell(x)e^{i\omega t} \tag{18}$$

$$j_-(x)e^{i\omega t} = -D_0\frac{\partial\eta_-}{\partial x}e^{i\omega t}-\mu\eta_-(x)E_\ell(x)e^{i\omega t} \tag{19}$$

The derivatives of the ionic currents over the distance *x,* with the help of the continuity equations, lead to,

$$-D_0\frac{\partial^2\eta_+}{\partial x^2}+\mu\frac{\partial\eta_+}{\partial x}E_\ell(x)+\mu\eta_+\frac{\partial E_\ell(x)}{\partial x} = -i\omega\eta_+(x) \tag{20}$$

$$-D_0\frac{\partial^2\eta_-}{\partial x^2}-\mu\frac{\partial\eta_-}{\partial x}E_\ell(x)-\mu\eta_-\frac{\partial E_\ell(x)}{\partial x} = -i\omega\eta_-(x) \tag{21}$$

From the Eqns. (18-21), we get the following second order differential equations for ionic densities,

$$\frac{\partial^2\eta_+}{\partial x^2}-\left(\frac{1}{2\lambda^2}\frac{\eta_+}{n_0}+\frac{i\omega}{D_0}\right)\eta_+ + \frac{1}{2\lambda^2}\frac{\eta_+}{n_0}\eta_(x) - \frac{q}{k_BT}E_\ell(x)\frac{\partial\eta_+}{\partial x} = 0 \tag{22}$$

$$\frac{\partial^2\eta_-}{\partial x^2}-\left(\frac{1}{2\lambda^2}\frac{\eta_-}{n_0}+\frac{i\omega}{D_0}\right)\eta_- + \frac{1}{2\lambda^2}\frac{\eta_-}{n_0}\eta_+ + \frac{q}{k_BT}E_\ell(x)\frac{\partial\eta_-}{\partial x} = 0 \tag{23}$$

To solve these differential equations, we make the following two simplifying assumptions. First, we assume that ionic concentrations have exponential profiles under high fields as a function of

the distance *x*. Second, we consider the Drude-like[41] response to the field frequency from the ions.

For the exponential distributions of ions, we use the following profiles,

$$\eta_+(x) = A\left(e^{Bx} - 1\right), \qquad \eta_-(x) = A\left(e^{B(d-x)} - 1\right) \tag{24}$$

where the constants A and B should be obtained from the boundary conditions. Putting these concentrations into Eqns. (22-23) and accepting that at the position $x=0$ (which is the left side boundary of the film), the local field obeys $E_\ell(0)=|V_0|/d$, we get the following expression for the constant B,

$$B = \frac{qV_0}{k_B T d} \tag{25}$$

The constant A is defined from the normalization of ionic concentration profiles $\eta_+(x)$ and $\eta_-(x)$ as,

$$\frac{1}{d}\int_0^d \eta_+(x)dx = n_0 \tag{26}$$

$$\frac{1}{d}\int_0^d \eta_-(x)dx = n_0 \tag{27}$$

which gives,

$$A = \frac{dB}{e^{dB} - dB - 1} n_0 \tag{28}$$

By introducing a dimensionless constant $K = q|V_0|/(k_B T) = dB > 0$, ionic concentrations given by Eqn. (24) can be written as,

$$\eta_+(x) = n_0 \frac{K}{e^K - K - 1}\left(e^{K\bar{x}} - 1\right) \tag{29}$$

$$\eta_-(x) = n_0 \frac{K}{e^K - K - 1}\left(e^{K(1-\bar{x})} - 1\right) \tag{30}$$

where $\bar{x} = x/d$. These profiles are written for a negative potential $-|V_0|<0$, which implies that the corresponding local field, $E_\ell(x)$, is directed from the left to the right (see Scheme 1B). For the positive potential $V_0>0$, the constant $K = qV_0/(k_B T) = dB$ is still positive and the ionic profiles

read,

$$\eta_+(x) = n_0 \frac{K}{e^K - K - 1}\left(e^{K(1-\bar{x})} - 1\right) \tag{31}$$

$$\eta_-(x) = n_0 \frac{K}{e^K - K - 1}\left(e^{K\bar{x}} - 1\right) \tag{32}$$

Using exponential profiles for ionic concentrations from Eqs. (29-31), we obtain the local field inside the PVDF layer,

$$E_\ell(x) = \frac{q}{\epsilon_m \epsilon_0}\int_0^x (\eta_+(\beta) - \eta_-(\beta))\, d\beta + C \tag{33}$$

which, after integration, produces,

$$E_\ell(x) = \frac{2dqn_0}{\epsilon_m \epsilon_0}\frac{1}{e^K - K - 1}\left(\cosh(K\bar{x}) - 1\right) + C \tag{34}$$

Consequently, the local potential inside the PVDF layer, given by the expression:

$$\phi(x) = -\int_0^x E_\ell(\beta) d(\beta) \tag{35}$$

we have,

$$\frac{q\phi(x)}{k_B T} = -\frac{1}{e^K - K - 1}\frac{1}{K}\left(\frac{d}{\lambda}\right)^2\left(\sinh(K\bar{x}) - K\bar{x}\right) - \frac{Cq}{k_B T}x \tag{36}$$

The constant C has to be defined from the boundary condition: $\varphi(x=d) = V_0$, thus

$$\frac{Cqd}{k_B T} = -\frac{qV_0}{k_B T} - \frac{1}{e^K - K - 1}\frac{1}{K}\left(\frac{d}{\lambda}\right)^2\left(\sinh(K) - K\right) \tag{37}$$

The final equation for the local potential in the middle PVDF layer reads,

$$\frac{q\phi(\bar{x})}{k_B T} = \frac{qV_0}{k_B T}\bar{x} + \frac{1}{e^K - K - 1}\frac{1}{K}\left(\frac{d}{\lambda}\right)^2\left(\bar{x}\sinh(K) - \sinh(K\bar{x})\right) \tag{38}$$

It is seen that the total potential drop is $\varphi(x)=V_0$ for $\bar{x} = 1$ at the boundary of the PVDF layer.

We construct new frequency dependent ionic profiles similar to the Drude relaxation model

for the ionic conductivity with the relaxation time, $\tau=\lambda^2/D$,[41]

$$\eta_+(x,\omega) = \frac{\eta_+(x) - n_0}{1 + i\omega\tau} + n_0 \tag{39}$$

$$\eta_-(x,\omega) = \frac{\eta_-(x) - n_0}{1 + i\omega\tau} + n_0 \tag{40}$$

Note that at $\omega = 0$, $\eta_+(x,0) = \eta(x)$, with both profiles being normalized to n_0; see Eqs. (26-27). At high ω values, $\eta_+(x,\infty) = \eta_0$. Similar relationships are also valid for the negative ions.

With the frequency-dependent profiles established for $\eta_+(x,\omega)$ and $\eta_-(x,\omega)$, the total charge in the film, which is defined in Eqn. (12), has the following distribution,

$$\rho_i(x,\omega) = qn_0 \frac{K}{\sinh(\frac{K}{2}) - \frac{K}{2}e^{-\frac{K}{2}}} \sinh\left(K\bar{x} - \frac{K}{2}\right) \frac{1}{1 + i\omega\tau} \tag{41}$$

Therefore, for the ionic polarization, $P_{ion}(\omega)$, of the PVDF layer, we get,

$$P_{ion}(\omega) = qn_0 d \frac{\cosh\left(\frac{K}{2}\right) - \frac{2}{K}\sinh\left(\frac{K}{2}\right)}{\sinh\left(\frac{K}{2}\right) - \frac{K}{2}e^{-\frac{K}{2}}} \frac{1}{1 + i\omega\tau} \tag{42}$$

It is worth noting that under a strong poling field, the constant $K\rightarrow\infty$, and thus the ionic polarization of the middle PVDF layer has an upper limit, $P_{ion}^{max} = q\ n_0\ d$. Also, the P_{ion} gives rise to the PVDF/HTPC boundary a space charge density, $\sigma_{sp} = P_{ion}$. Note, the constant, $K = |qV_0/(k_BT)| > 0$, is always positive, regardless of the polarity of the voltage V_0 applied to the PVDF layer.

Determination of $\varepsilon_{ion}(\omega)$ from ionic polarization of the PVDF layer, $P_{ion}(\omega)$. The full polarization of a single dielectric layer under the applied field, E_0, in Scheme 1A is determined as:

$$\vec{P}_{full} = \epsilon_0(\epsilon_{full} - 1)\vec{E}_0 = \vec{P}_m + \vec{P}_{ion} = \epsilon_0(\epsilon_m - 1)\vec{E}_0 + \epsilon_0\epsilon_{ion}\vec{E}_0 \tag{43}$$

where we separate the matrix ε_m and ionic ε_{ion} contributions to the total permittivity ($\varepsilon_{full} = \varepsilon_m + \varepsilon_{ion}$), and thus the matrix polarization (P_m) and the ionic polarization (P_{ion}) to the total polarization

of the PVDF layer, P_{full}. The ionic polarization of the PVDF layer is defined as

$$P_{ion} = \varepsilon_0 \varepsilon_{ion} E_0 \quad (44)$$

The frequency dependent ionic permittivity is calculated as the Fourier transformation of P_{ion},

$$\epsilon_{ion}(\omega) = \frac{1}{\epsilon_0 E_0} \frac{\omega}{\pi} \int_0^{\frac{2\pi}{\omega}} P_{ion}(t) e^{-i\omega t} dt \quad (45)$$

Using $P_{ion}(t) = P_{ion}(\omega) e^{i\omega t}$, Eqn. (45) is simplified to

$$\epsilon_{ion}(\omega) = \frac{P_{ion}(\omega)}{\epsilon_0 E_0} = \frac{D(\omega)}{\epsilon_0 E_0} \quad (46)$$

According to Eqn. (46), $P_{ion}(\omega) = D(\omega) = \sigma_{sp}$.

In the case of the HTPC/PVDF/HTPC trilayer film placed under an external potential, V_0 (see Scheme 1B), Eqn. (46) for the calculation of $\varepsilon_{ion}(\omega)$ has to be modified, because both single layer quantities $P_{ion}(\omega)$ and E_0 in Eqn. (46) depend on the parameters of the boundary HTPC layer. The details of such dependence can be found in our previous report.[25]

The electric field E_1 in the HTPC layer and the electric field E_2 in the PVDF layer are defined as,

$$E_1 = \frac{\varepsilon_0 \varepsilon_m V_0 + P_{ion}(\omega) d}{\varepsilon_0 (\varepsilon_1 d + 2\varepsilon_m d_1)} \quad (47)$$

$$E_2 = \frac{\varepsilon_0 \varepsilon_1 V_0 - P_{ion}(\omega) 2d_1}{\varepsilon_0 (\varepsilon_1 d + 2\varepsilon_m d_1)} \quad (48)$$

where d_1 is the thickness of the HTPC layer and V_0 is the total voltage applied on the trilayer. Note that, the fields E_1 and E_2 have no dependence on the distance x in the PVDF layer. Thus, the field E_2, different from the local field $E_\ell(x)$ in Eq. (34), is a macroscopic average field. In other words, E_2 can be calculated as the integrated average of $E_\ell(x)$ in the PVDF film. The electric displacement in the HTPC layer, $D_1(\omega) = \varepsilon_0 \varepsilon_1 E_1(\omega)$, which also has a macroscopic nature, can be written as:

$$D_1(\omega) = \frac{\varepsilon_0\varepsilon_1\varepsilon_m V_0 + 2a\varepsilon_1 P_{ion}(\omega)}{2a\varepsilon_1 + 2d_1\varepsilon_m} \quad (49)$$

It has a dipolar polarization part, $D^{(d)}{}_1(\omega)$:

$$D_1^{(d)}(\omega) = \frac{\varepsilon_0\varepsilon_1\varepsilon_m V_0}{2a\varepsilon_1 + 2d_1\varepsilon_m} \quad (50)$$

and an ionic polarization part, $D^{(i)}{}_1(\omega)$:

$$D_1^{(i)}(\omega) = \frac{2a\varepsilon_1 P_{ion}(\omega)}{2a\varepsilon_1 + 2d_1\varepsilon_m} \quad (51)$$

The total charge on the electrodes is $\sigma(\omega) = D_1^{(d)}(\omega) + D_1^{(i)}(\omega)$, and the ionic permittivity reads,

$$\varepsilon_{ion}(\omega) = \frac{D_1^{(i)}(\omega)}{\varepsilon_0 E_0} = \frac{d\varepsilon_1}{d\varepsilon_1 + 2d_1\varepsilon_m}\frac{P_{ion}(\omega)}{\varepsilon_0 E_0} \quad (52)$$

Note that there is an interdependence between the ionic polarization $P_{ion}(\omega)$ and the field E_2 in the PVDF layer. Therefore, they should be stabilized through iterations as explained below.

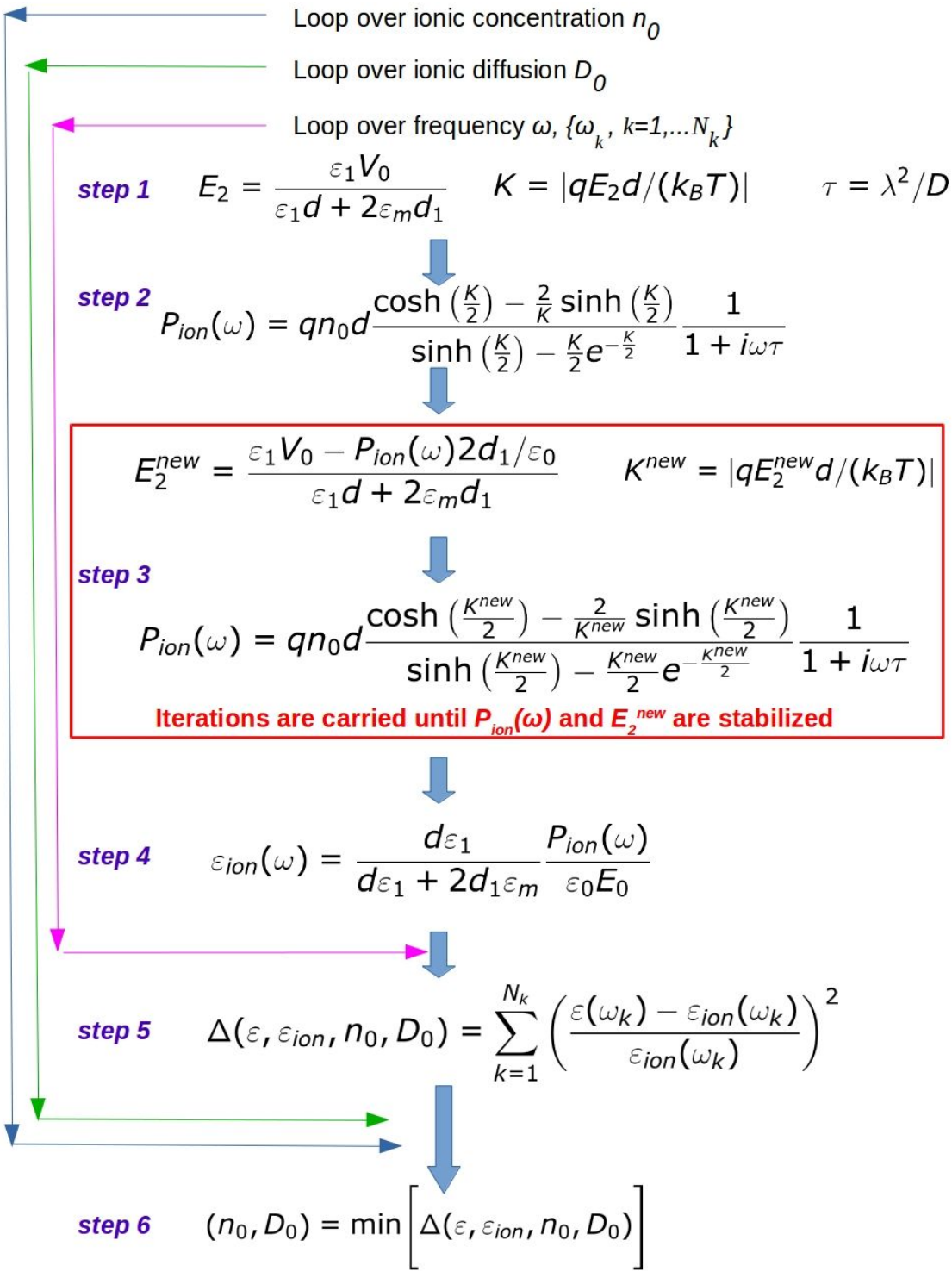

Scheme 2. Schematic iteration procedure to determine n_0 and D_0 of impurity ions in the middle PVDF layer in the HTPC/PVDF/HTPC trilayer. The six steps of this iteration procedure are discussed in the main text.

Fitting experimental data of $\varepsilon_{ion}(\omega)$ through iterations

The fitting procedure is explained in Scheme 2 for approach II (the fitting procedure for approach I is almost the same). First, three loops start for certain initial values of n_0, D_0 at a given ω of the alternating field. Then, as a first step, we calculate the field E_2 in the PVDF layer without any ion transport, which corresponds to the zero diffusion of ions. In the second step, we calculate $P_{ion}(\omega)$ with the ionic diffusion taking into account. Using this polarization, we update the non-ionic E_2 to the ionic E_2^{new}, and recalculate the ionic $P_{ion}(\omega)$ again. Note that, the macroscopic field E_2^{new}, like the field E_2, is the integrated average of $E_\ell(x)$. Also note that, the sign of E_2^{new} might be reversed from positive to negative if a high ion polarization (corresponding to significant electric double layers formed at the PVDF/HTPC boundaries) takes place in the highly ionized PVDF film in a strong external field. In this case, however, the HTPC macroscopic field E_1 will become more positive in order to compensate for the potential hiking in the PVDF layer. This iterative procedure, i.e., the step 3 in Scheme 2, is repeated until both E_2^{new} and $P_{ion}(\omega)$ are stabilized. In step 4, we define $\varepsilon_{ion}(\omega)$. In step 5, we calculate the deviation of $\varepsilon_{ion}(\omega)$ from $\varepsilon(\omega)$ for n_0 and D_0. All these deviations are stored, and in step 6 we define the minimum deviation. The ionic parameters corresponding to this deviation are treated as the best fit for n_0 and D_0. At high frequencies, finding the best fit parameters becomes ambiguous because of the reduced contribution of ions to $\varepsilon_{ion}(\omega)$. That is why fitting parameters $n_0(\omega)$ and $D_0(\omega)$ have larger errors at high frequencies.

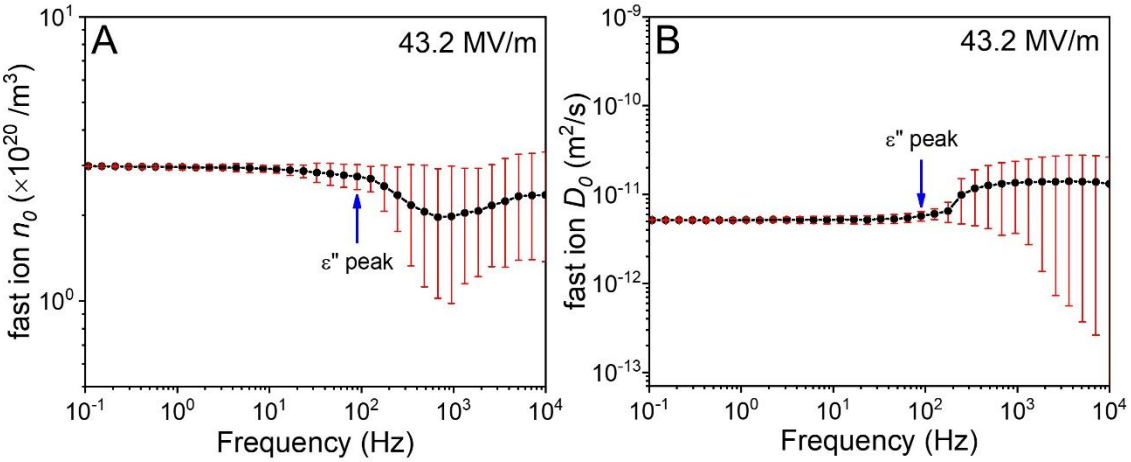

Figure 4. Simulated (A) n_0 and (B) D_0 as a function of frequency at 43.2 MV/m and 130 °C using approach II. The increased error bars above the ε″ peak frequency indicates that the fitting becomes ambiguous at higher frequencies.

Simulated n_0 and D_0 at 43.2 MV/m and 130 °C using approach II are shown as a function of frequency in Figures 4A and B, respectively. Errors in n_0 and D_0 became larger when the frequency was above the ε'' peak frequency. This is attributed to the fact that impurity ions stop moving at high frequencies. The values at the ε'' peak frequency were chosen for the final simulation results.

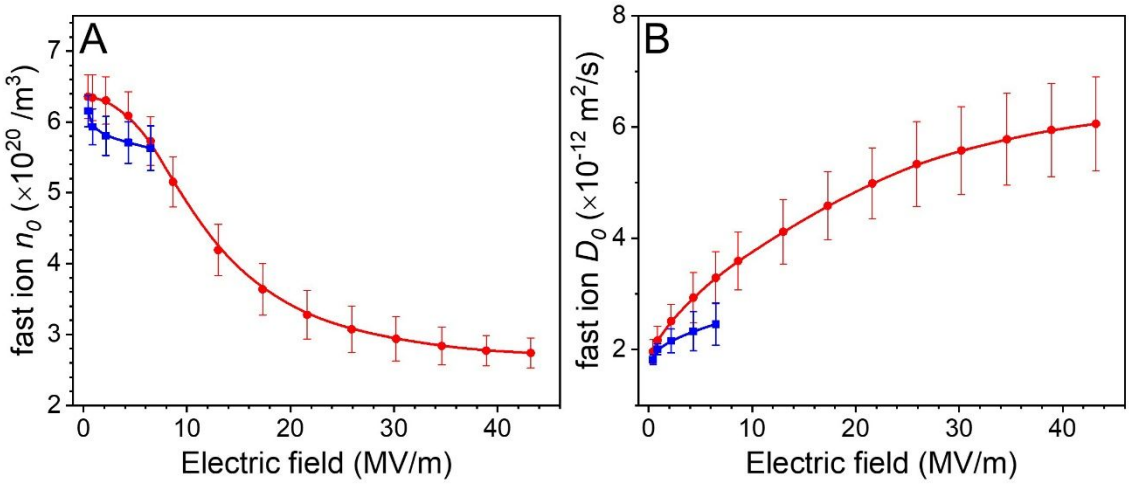

Figure 5. Simulated (A) n_0 and (B) D_0 as a function of the amplitude of AC field at 130 °C. Blue symbols represent results using approach I, which is applicable up to 6 MV/m. Red symbols represent results using approach II.

The simulated n_0 and D_0 of the fast ions as a function of the applied AC field (with an amplitude of E_0) at 130 °C are shown in Figure 5. Note, approach I only worked up to 6 MV/m, above which the concentration of positive ions at the PVDF boundary under the highest voltage, and the concentration of negative ions at the PVDF boundary under the lowest voltage became larger than the average concentration n_0. This resulted in unphysical negative ionic concentrations at the corresponding boundaries. Instead, approach II worked well under all electric fields, because accumulation of ions was observed for $E_0 > 6$ MV/m. Upon increasing E_0, n_0 decreased and D_0 increased. The decrease of n_0 with E_0 could be explained by the reduced number of mobile ions after a significant fraction was blocked by the HTPC/PVDF interfaces upon high field and low frequency poling. The increase of D_0 with E_0 was a result of increasing driving force for impurity ions to move in the PVDF layer.

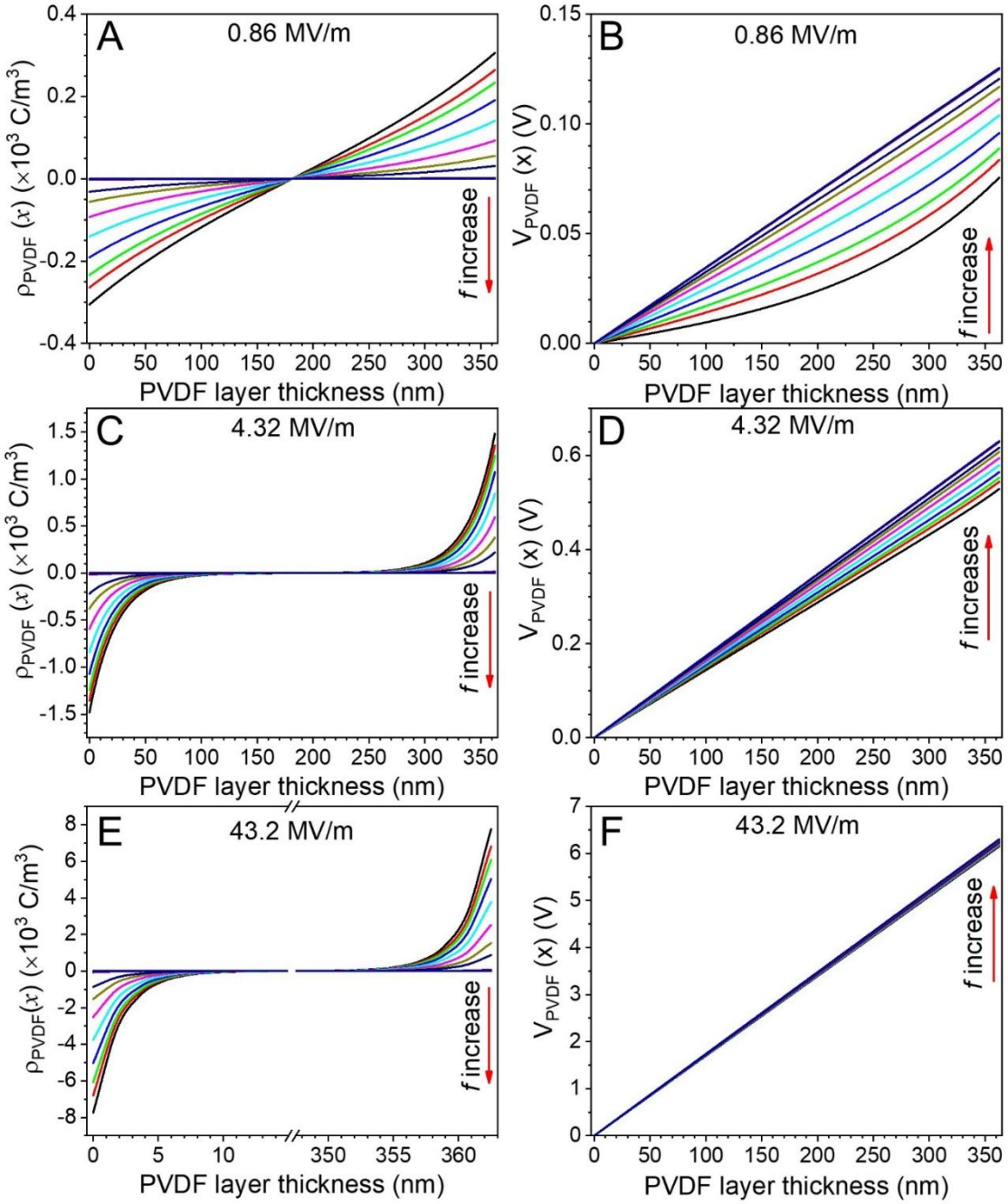

Figure 6. (A,C,E) Charge density of fast ions [$\rho_{PVDF}(x)$] and (B,D,F) voltage profiles [$V_{PVDF}(x)$] under different applied E_0, (A,B) 0.86 MV/m, (C,D) 4.3 MV/m, and (E,F) 43.2 MV/m, for the HTPC/PVDF/HTPC trilayer at 130 °C. The simulation method is approach II. Different frequencies are: 0.5, 8, 11, 16, 23, 32, 45, 64, 246, 677, 1859, 7142 Hz.

The fast-ion charge density profile [$\rho_{PVDF}(x)$] and voltage profile, $V_{PVDF}(x)$, in the confined PVDF layer under various applied AC fields (0.86, 4.3, and 43.2 MV/m) at 130 °C are shown in

Figure 6. When E_0 = 0.86 MV/m, $\rho_{PVDF}(x)$ became larger across the entire PVDF layer as the frequency decreased, indicating the enhanced conduction of impurity ions at lower frequencies (Figure 6A). As a result, $V_{PVDF}(x)$ gradually deviated from the linear relationship (Figure 6B). When E_0 increased to 4.3 MV/m, ions were more polarized to accumulate at the HTPC/PVDF interfaces (Figure 6C). Again, $V_{PVDF}(x)$ slightly deviated from the linear relationship as frequency decreased (Figure 6D). When E_0 reached as high as 43.2 MV/m, most ions were polarized to the HTPC/PVDF interfaces, i.e., within 10 nm (or 3%) of the PVDF layer thickness (Figure 6E). As a result, the amount of free impurity ions that could conduct in the PVDF layer was little. Consequently, $V_{PVDF}(x)$ became nearly linear under all frequencies (Figure 6F). The high-field charge density profile in Figure 6E is quite similar to the case of EDL;[5] however, the voltage drop profile in Figure 6F is different. For the EDL, the voltage drop only happens within the EDL and the voltage drop in the bulk is nearly zero.[5] The different voltage profile for the HTPC/PVDF/HTPC trilayer under high fields can be explained by the ultralow n_0 of the fast ions ($\sim 10^{21}/m^3$), as compared to the dipole (i.e., repeat unit) density of PVDF ($1.7\times10^{28}/m^3$, given the density of PVDF is around 1.8 g/cm^3). Given such a low ion concentration, the polarized ions cannot generate a high enough inverse field to reduce the local field in the bulk PVDF layer to zero.

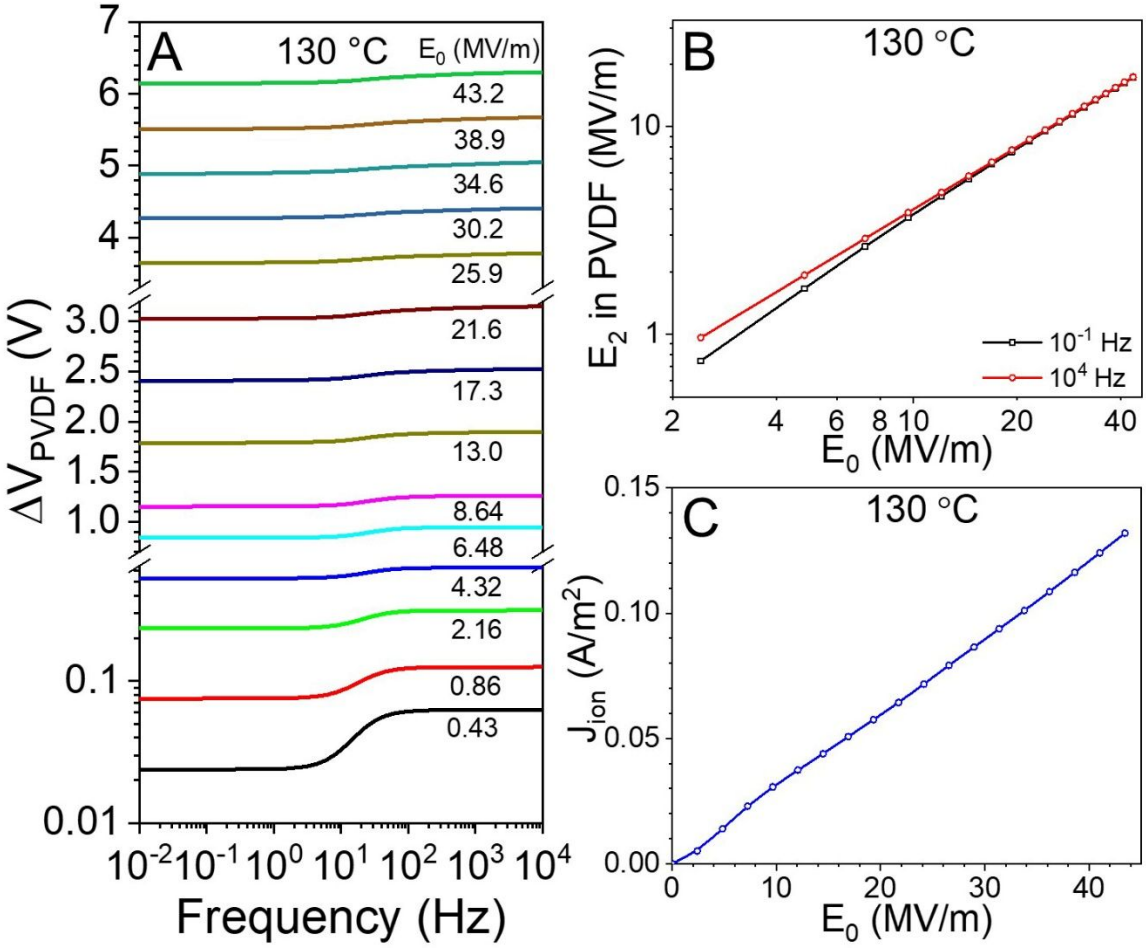

Figure 7. (A) Voltage drop (ΔV_{PVDF}) in the PVDF layer as a function of frequency under different AC electric fields (the amplitude is E_0) at 130 °C. (B) Average electric field E_2 in the PVDF layer at 10^{-1} and 10^4 Hz, respectively, and (C) ionic current density (J_{ion}) at 10^{-1} Hz as a function of E_0. Results are obtained from approach II simulation.

From the voltage profiles in Figure 6, the voltage drops (ΔV_{PVDF}) under different frequencies at 130 °C could be obtained, as seen in Figure 7A. At high frequencies (>10^3 Hz), when the ions are practically immobile, ΔV_{PVDF} reaches its higher plateau values. As frequency decreased, ΔV_{PVDF} had a stepwise decrease around 20 Hz for all applied AC electric fields. This is attributed to the impurity ion conduction in the PVDF layer, which is consistent with a previous phenomenological study.[26] By dividing ΔV_{PVDF} with the PVDF layer thickness, the average electric field E_2 was obtained (Figure 7B). As expected, at a low E_0, the E_2 values at low (10^{-1} Hz) and high frequencies (10^4 Hz) were different. Upon increasing E_0, the difference became

increasingly smaller, because most of the ions were polarized to the HTPC/PVDF interfaces and fewer mobile ions could conduct. Since $J_{ion} = \sigma_{ion}E_2$, $\sigma_{ion} = qn_0\mu$, and $\mu = qD_0/kT$, $J_{ion} = q^2n_0D_0E_2/kT$, where J_{ion} is ionic current density, σ_{ion} ionic conductivity, q charge of fast ions, μ ion mobility, k Boltzmann constant, and T temperature. J_{ion} as a function of E_0 is shown in Figure 7C. As E_0 increased, J_{ion} increased monotonically, with a slight deviation from the linear relationship when the applied field is lower than 8 MV/m. The increase in J_{ion} was largely a result of increased E_2 and D_0, although n_0 decreased with E_0.

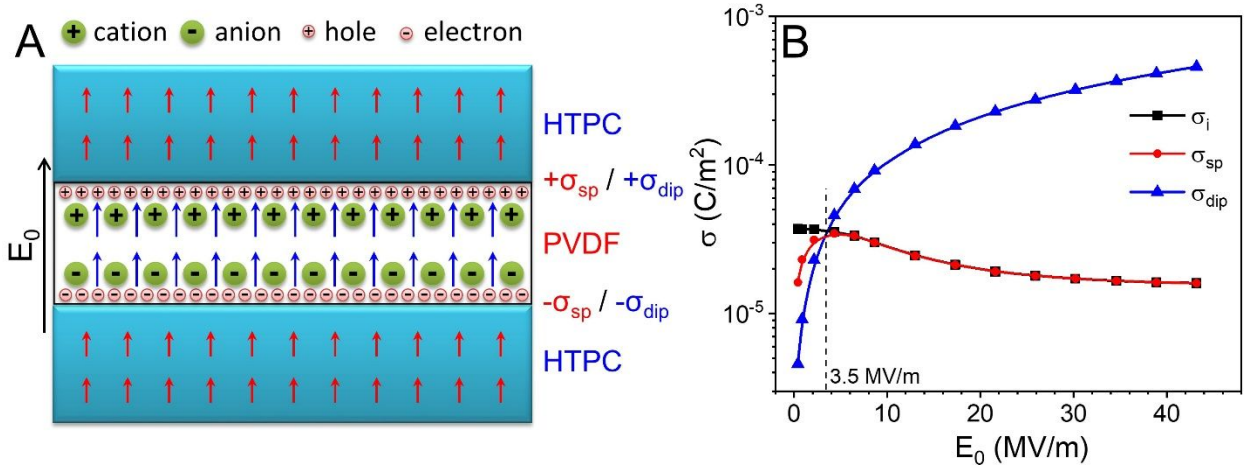

Figure 8. (A) Schematic representation of space charge (σ_{sp}) and dipolar interfacial polarizations (σ_{dip}) in the HTPC/PVDF/HTPC trilayer under an applied electric field. Space charges include both thermally activated electrons and impurity ions in PVDF. Supposedly, no free holes should exist for insulators. The holes are shown in the scheme as image charges to compensate the polarized electrons. (B) σ_i, σ_{sp}, and σ_{dip} as a function of the applied AC electric field E_0. Here, σ_i is the interfacial charge density when all n_0 ions are accumulated at the HTPC/PVDF interfaces. σ_{sp} is the interfacial charge density, from which the ΔV_{PVDF} is generated. The difference between σ_i and σ_{sp} indicates that ions must have a diffuse distribution in the PVDF layer. σ_{dip} is the dipolar interfacial charge density.

When an electric field is applied to the HTPC/PVDF/HTPC trilayer, both space charge (σ_{sp}) and dipolar interfacial polarizations (σ_{dip}) take place, as depicted in Figure 8A. This is a result of large contrasts in (ionic and electronic) conductivity and permittivity between HTPC and PVDF.[23] Usually, the concentration of thermally activated electrons is rather low (in the order

of 10^{15} /m^3),[42] about 10^6 times lower than the concentration of impurity ions. Therefore, the contribution of thermally activated electrons to σ_{sp} can be ignored. Figure 8B shows the results for dipolar and space charge interfacial polarizations as a function of the external AC field, E_0. First, we define σ_i as the interfacial charge density when all n_0 ions are condensed at the HTPC/PVDF interfaces, and σ_{sp} as the interfacial charge density that generates ΔV_{PVDF} at low frequencies (e.g., 10^{-1} Hz) as shown in Figure 7A. Below 4 MV/m, σ_i and σ_{sp} were different, and this is attributed to the diffuse distribution of fast ions in the PVDF layer (see Figure 6A). Above 4 MV/m, σ_i and σ_{sp} became nearly the same, indicating all fast ions were polarized to the HTPC/PVDF interfaces at low frequencies under high electric fields. Second, σ_{dip}, which is equal to the dielectric displacement $D^{(d)}_1$, can be obtained from Eqn. 50. Below 3.5 MV/m, σ_{dip} is smaller than σ_{sp}. Above 3.5 MV/m, σ_{dip} monotonically increased and became significantly higher than σ_{sp} as E_0 increased. This is attributed to the much higher concentration of VDF dipoles (1.7×10^{28} /m^3) than impurity ions (~10^{21} /m^3), and the high electric field dramatically increased the dipolar polarization for PVDF.

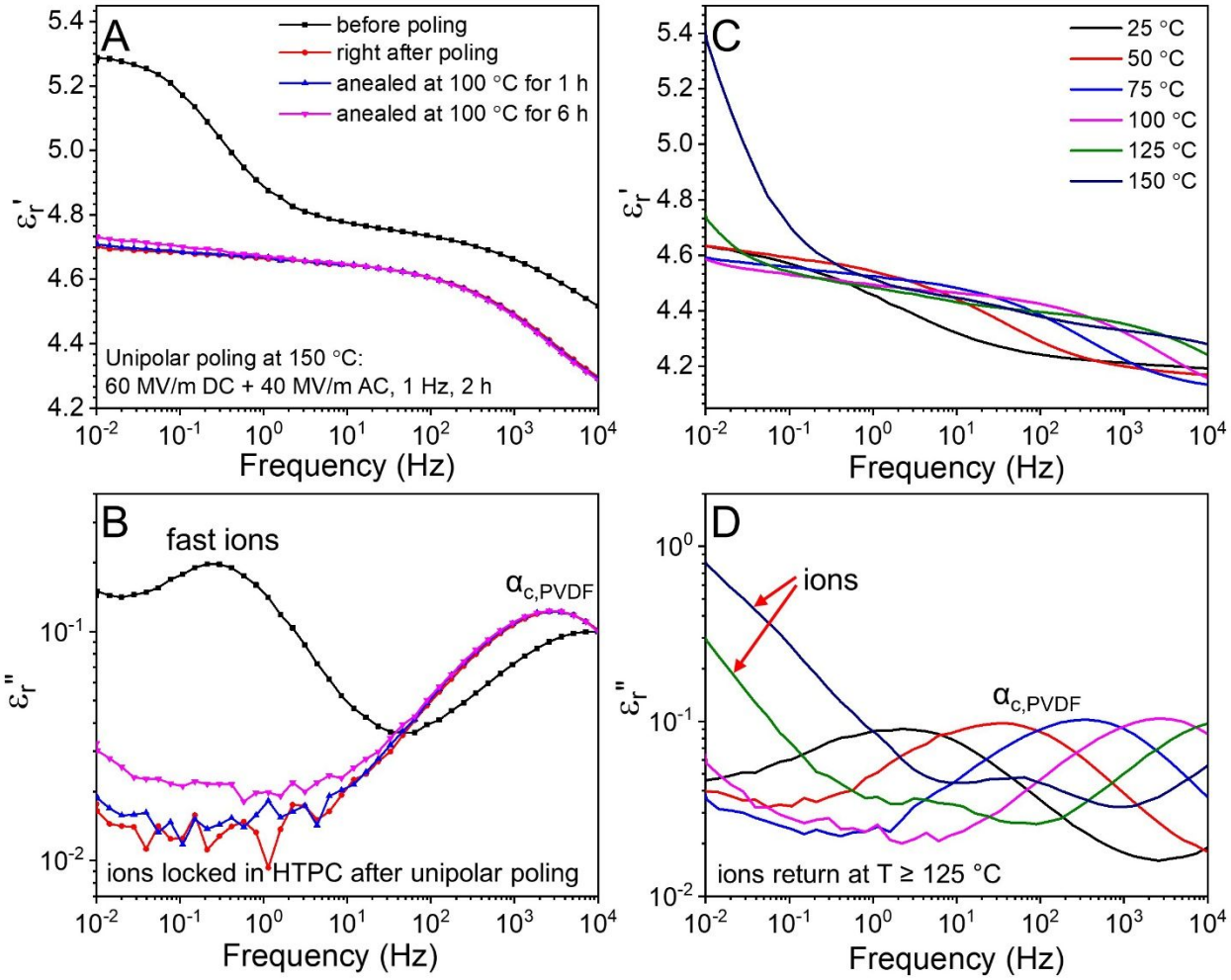

Figure 9. Frequency-scan HV-BDS results of (A) ε_r' and (B) ε_r'' for the HTPC/PVDF 50/50 33L film at 100 °C before and after electric poling at 150 °C. After poling, the sample was further annealed at 100 °C for 1 and 6 h to study how fast the polarized impurity ions relax. Frequency-scan HV-BDS results of (C) ε_r' and (D) ε_r'' for the poled HTPC/PVDF 50/50 33L film at different temperatures. The poling condition was 60 MV/m DC + 40 MV/m AC at 1 Hz and 150 °C for 2 h.

Determination of optimal poling conditions to drive fast ions into the HTPC layers and thermal stability of the locked impurity ions

The above analytical simulation of ion transport in the HTPC/PVDF 50/50 33L film can help us determine optimal poling conditions for driving impurity ions into the HTPC layers. First, the poling temperature should be close enough to the T_g of HTPC (i.e., 165 °C) so that HTPC becomes soft enough for the impurity ions to enter its matrix. In this study, we chose 150 °C for electric

poling, which was 15 °C below the T_g of HTPC. Heating above the T_g of HTPC should be avoided for poling, because the surface HTPC layers tended to break up, resulting in poor quality films with easy dielectric breakdown. Second, we should compare the effects of different poling modes, i.e., AC (or bipolar), DC, or AC+DC (or unipolar) poling. The AC or bipolar poling should be the least considered because impurity ions will be polarized back and forth during one poling cycle. This will not easily drive impurity ions into the HTPC layers. The DC poling might not be the best method, because the ΔV_{PVDF} decreases to a lower level under a DC field (see Figure 7A at low frequencies). Holding at a high DC electric field also increased the chance of dielectric breakdown at high temperatures. The AC+DC (or unipolar) poling should be the most desired, because impurity ions will be polarized in one direction to enter the HTPC layers. Third, the poling frequency should be below the critical frequency so that fast ions could fully move. Based on the results in Figure 7A, we choose a frequency of 1 Hz to make sure the complete conduction of fast ions.

Taking these considerations into account, we carried out detailed studies to determine the optimal poling conditions to drive the fast ions into HTPC layers. Figure S3 compares the poling effect for AC, DC, and AC+DC poling methods. Figure S4 compares different electric fields for the AC+DC method. Figure S5 compares different poling times for the AC+DC method. Based on these results, the optimal electric poling conditions were chosen, namely, 60 MV/m DC + 40 MV/m AC at 1 Hz and 150 °C for 2 h. The slightly higher DC field is to make sure that no ions could drift back in the opposite direction during the poling process. Figures 9A and B show the HV-BDS results of ε_r' and ε_r'' at 100 °C before and after the 150 °C-poling process. Right after poling, the fast ion peak in ε_r'' disappeared. After annealing at 100 °C for 1 h, there was nearly no change in the ε_r'', suggesting the successful locking of impurity ions in the HTPC layers. After

annealing at 100 °C for 6 h, there was only a slight increase of the ε_r'' at low frequencies, suggesting minor returning or relaxation of the locked fast ions. SAXS and WAXD data are shown in Figure S6. Judging from the WAXD patterns, edge-on α PVDF crystals confined in the MLF were observed. After high-field electric poling, no phase transition or orientation change could be detected. This indicates that the decreased dielectric loss at low frequencies should not be caused by the changes in PVDF crystals, but caused by the polarized and locked impurity ions. The thermal stability of the locked fast ions in the HTPC layers was studied by frequency-scan HV-BDS after quenching the 150 °C-poled HTPC/PVDF 33L film to room temperatures. As we can see, the low-frequency impurity ion peak in ε_r'' did not come back until 125 °C (Figure 9D), suggesting that the thermal stability of the locked fast ions in the HTPC layers should be up to 125 °C.

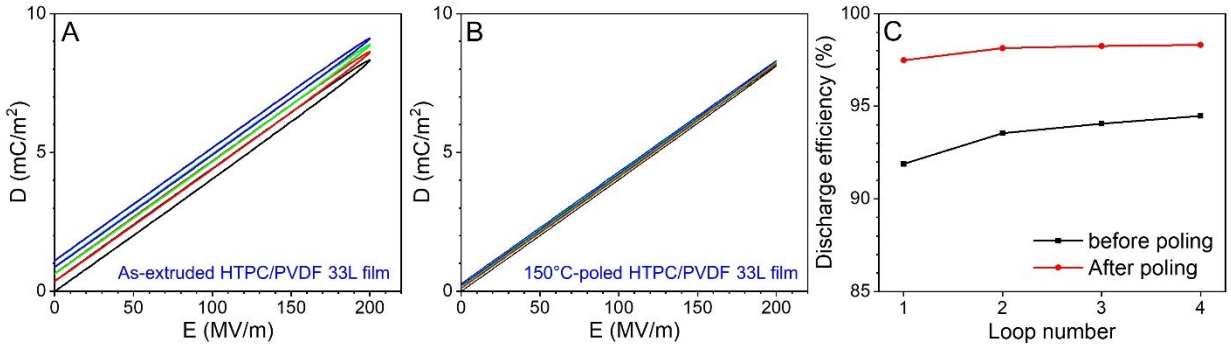

Figure 10. Comparison of four continuous unipolar D-E loops at 100 °C for (A) the as-extruded and (B) 150 °C-poled HTPC/PVDF 50/50 33L films. (C) Discharge efficiency as a function of the unipolar poling number for the as-extruded and 150 °C-poled HTPC/PVDF 50/50 33L films. The poling frequency was 1 Hz with a sinusoidal wave function.

Locked interfacial charges for improved dielectric properties of HTPC/PVDF MLFs

With locked interfacial ions in the glassy HTPC layers, we expect that dielectric properties would be improved for the HTPC/PVDF MLFs. Unipolar D-E loops were used to demonstrate the

decrease of dielectric loss at high electric fields for the poled HTPC/PVDF MLF. Note, bipolar D-E loop tests should be avoided because the reverse high field would have a chance to detrap the fast ions from the HTPC layers. Figures 10A and B show the comparison of D-E loops for the as-extruded and 150 °C-poled HTPC/PVDF 50/50 33L films. It was clear that the 150 °C-poled film exhibited significantly improved discharge efficiency (Figure 10C).

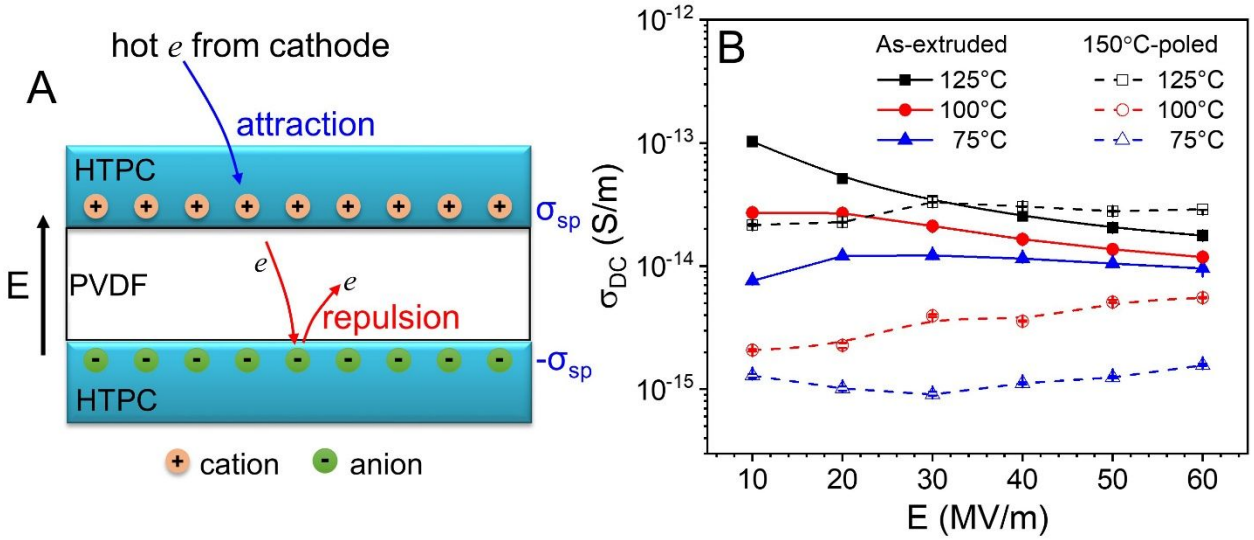

Figure 11. (A) Schematic representation of locked interfacial charges as barriers to prevent cathode-injected hot electrons from penetrating through the HTPC/PVDF MLF. (B) Bulk DC conductivity (σ_{DC}) as a function of electric field for the as-extruded and 150 °C-poled HTPC/PVDF 50/50 33L films at different temperatures, as determined by the leakage current measurements.

The locked interfacial ionic charges can build electrical barriers to prevent cathode-injected hot electrons from penetrating through the MLF, thus decreasing the leakage current and potentially increasing the breakdown strength. As shown in the schematic representation (Figure 11A), the injected hot electrons will be trapped by the layer of cations and repelled by the layers of anions in the poled HTPC/PVDF MLF. Figure 11B shows bulk DC conductivity (σ_{DC}) as a function of the electric field for the poled MLF at 75, 100, and 125 °C, as compared to the as-extruded MLF. Because of the instrument limit of 1000 V_{DC}, the leakage current could only be

measured up to 60 MV/m in this study because the MLF thickness was ca. 12 μm. Note that this σ_{DC} included both electronic and ionic contributions to the DC conductivity. At 75 °C, the poled MLF exhibited one order of magnitude lower σ_{DC} than the as-extruded MLF. At 100 °C, the difference in σ_{DC} between the poled and as-extruded MLFs was large at 10 MV/m, but gradually became smaller as the field increased. At 125 °C, the σ_{DC} values for the poled and as-extruded MLFs quickly became similar above 30 MV/m. At temperatures above 100 °C, the σ_{DC} for the as-extruded MLF gradually decreased with increasing the electric field. This had been attributed to the continuous poling of impurity ions to the HTPC/PVDF interfaces to reduce ionic conduction in the system.[26] As a result, the σ_{DC} values for the as-extruded MLF became similar to those of the poled MLF at a high enough field.

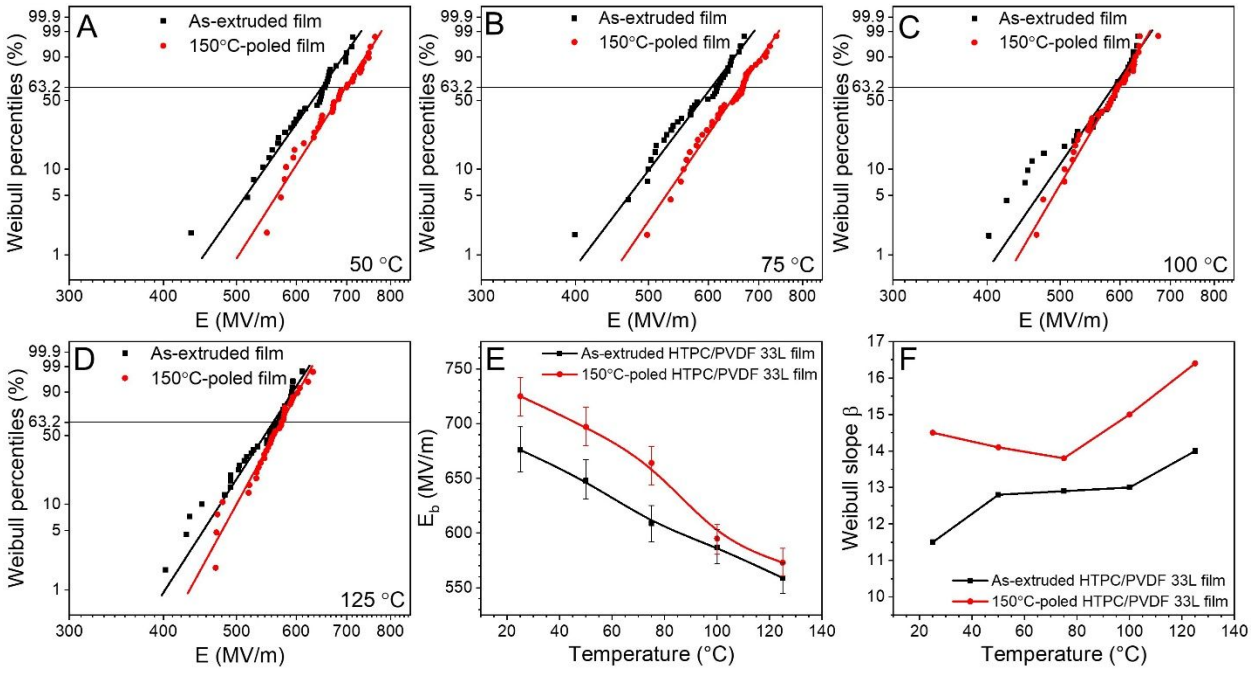

Figure 12. Weibull analysis plots of breakdown strength for as-extruded and 150 °C-poled HTPC/PVDF 33L films at (A) 50 °C, (B) 75 °C, (C) 100 °C and (D) 125 °C. Summarized Weibull (E) breakdown strength (E_b) and (F) slope (β) for as-extruded and 150 °C-poled HTPC/PVDF 33L films at different temperatures. The error bars in (E) are obtained from standard deviation.

Figures 12A-D show the comparison of Weibull breakdown strengths for the as-extruded and 150 °C-poled MLFs. More than 30 samples were tested for each Weibull analysis to ensure meaningful statistics. Results of Weibull breakdown strength (E_b) and slope (β) are shown in Figures 12E and F, respectively. In general, the E_b gradually decreased upon increasing temperature for both poled and as-extruded MLFs because of enhanced conduction at elevated temperatures. However, when the temperature was ≤75 °C, the poled MLF exhibited about 50 MV/m higher breakdown strength than the as-extruded MLF. Above 100 °C, the difference in breakdown strength between the poled and as-extruded MLFs became smaller (Figure 12E), because the locked impurity ions started to be detrapped from HTPC at high enough temperatures. The Weibull slope β for the poled MLF was consistently higher than that for the as-extruded MLF (Figure 12F). This result demonstrated that the locked interfacial charges in the HTPC layers were beneficial for enhancing the ultimate breakdown strength for MLFs.

Conclusions

In this study, impurity ionic transport confined in HTPC/PVDF MLFs under high AC electric fields was investigated. Different from the confined ion transport under low electric fields, the classic ion distribution function based on the ion diffusion model failed to describe the significant poling effect under a high field. Taking advantage of the exponential distribution function of ions under a DC field,[5] we implemented a direct analytical modeling method to understand the confined ion transport in the HTPC/PVDF/HTPC trilayer. After iterative stabilization of the average field E_2 and $P_{ion}(\omega)$ in the PVDF layer, n_0 and D_0 were extracted by fitting the experimental HV-BDS data at 130 °C. It was observed that n_0 decreased whereas D_0 increased with increasing the electric field. The decrease of n_0 was explained by the decreased

amount of mobile ions after a significant fraction of ions were blocked by the HTPC layers. Unlike the situation under the low-field electric poling, the σ_{dip} became significantly larger than the σ_{sp} when the electric field increased to above 3.5 MV/m.

Given the understanding of confined ion transport under high electric fields, electric poling experiments were carried out to lock the fast impurity ions into the HTPC. The optimal poling conditions were determined to be 60 MV/m DC + 40 MV/m AC at 1 Hz and 150 °C for 2 h. After electric poling, the HTPC/PVDF MLF exhibited enhanced discharge efficiency, reduced leakage current, and improved dielectric breakdown strength when the temperature is below 100 °C. This was attributed to the polarized/locked impurity ions in the HTPC layers.

Acknowledgements

This work is supported by Office of Naval Research under grant No. N00014-19-1-2032. E.A. additionally acknowledges support of this work by the Deutsche Forschungsgemeinschaft (DFG) through the grant AL 2058/1-1. This work used the 11-BM CMS beamline of National Synchrotron Light Source-II (NSLS-II), Brookhaven National Laboratory (BNL), a U.S. Department of Energy User Facility operated for the Office of Science by BNL under Contract DE-SC0012704.

Electronic Supplementary Information (ESI) available: Melt viscosity for HTPC, PSF, and PVDF, calculation of the D-E loop at 100 °C, HN deconvoluted HV-BDS curves, determination of optimal electric poling conditions to lock impurity ions in the HTPC layers, and SAXS/WAXD patterns for the HTPC/PVDF MLF before and after high-field electric poling. See DOI: xxxxxxxxxxxxxxxx

References

1. D. Montanari, K. Saarinen, F. Scagliarini, D. Zeidler, M. Niskala and C. Nender, *Proceedings of CARTS U.S.A. 2009*, Jacksonville, FL, U.S.A., 2009.
2. W. J. Sarjeant, J. Zirnheld and F. W. MacDougall, *IEEE Trans. Plasm. Sci.*, 1998, **26**, 1368-1392.
3. W. J. Sarjeant, I. W. Clelland and R. A. Price, *Proc. IEEE.*, 2001, **89**, 846-855.
4. G. A. Snook, P. Kao and A. S. Best, *J. Power Sources*, 2011, **196**, 1-12.
5. J. O. M. Bockris, A. K. N. Reddy, M. E. Gamboa-Aldeco, *Modern Electrochemistry: Fundamentals of Electrodics*, Vol. 2A, 2nd Ed., Kluwer Academic, New York, 2002.
6. L. Zhu, *J. Phys. Chem. Lett.*, 2014, **5**, 3677-3687.
7. M. Ritamäki, I. Rytöluoto and K. Lahti, *2nd IEEE International Conference on Dielectrics (ICD)*, Budapest, Hungary, 2018.
8. M. Ritamäki, I. Rytöluoto and K. Lahti, *IEEE Trans. Dielectr. Electr. Insul.*, 2019, **26**, 1229-1237.
9. D. Tan, L. Zhang, Q. Chen and P. Irwin, *J. Electron. Mater.*, 2014, **43**, 4569-4575.
10. L. Schosseler, *Bodo's Power Systems*, 2016, 50-51.
11. Q. Li, F. Z. Yao, Y. Liu, G. Zhang, H. Wang and Q. Wang, *Annu. Rev. Mater. Res.*, 2018, **48**, 219-243.
12. S. Wu, W. Li, M. Lin, Q. Burlingame, Q. Chen, A. Payzant, K. Xiao and Q. M. Zhang, *Adv. Mater.*, 2013, **25**, 1734-1738.
13. S. Wu, Q. Burlingame, Z. X. Cheng, M. Lin and Q. M. Zhang, *J. Electron. Mater.*, 2014, **43**, 4548-4551.

14. Y. Thakur, B. Zhang, R. Dong, W. Lu, C. Iacob, J. Runt, J. Bernholc and Q. M. Zhang, *Nano Energy*, 2017, **32**, 73-79.

15. Y. Thakur, R. Dong, M. Lin, S. Wu, Z. Cheng, Y. Hou, J. Bernholc and Q. M. Zhang, *Nano Energy*, 2015, **16**, 227-234.

16. M. Mackey, D. E. Schuele, L. Zhu and E. Baer, *J. Appl. Phys.*, 2012, **111**, 113702.

17. L. Yang, E. Allahyarov, F. Guan and L. Zhu, *Macromolecules*, 2013, 46, 9698-9711.

18. E. Baer, A. Hiltner, J. S. Shirk and M. A. Wolak, Multilayer polymer dielectric film, US 20100172066A1, 2010, and US 20140160623A1, 2014.

19. D. Langhe and M. Ponting, *Manufacturing and Novel Applications of Multilayer Polymer Films*, Elsevier, Amsterdam, 2015.

20. M. A. Wolak, M. J. Pan, A. Wan, J. S. Shirk, M. Mackey, A. Hiltner, E. Baer and L. Flandin, *Appl. Phys. Lett.*, 2008, **92**, 113301.

21. M. Mackey, A. Hiltner, E. Baer, L. Flandin, M. A. Wolak and J. S. Shirk, *J. Phys. D: Appl. Phys.*, 2009, **42**, 175304.

22. M. Mackey, D. E. Schuele, L. Zhu, L. Flandin, M. A. Wolak, J. S. Shirk, A. Hiltner and E. Baer, *Macromolecules*, 2012, **45**, 1954-1962.

23. E. Baer and L. Zhu, *Macromolecules*, 2017, **50**, 2239-2256.

24. J. Ho and T. R. Jow, *Characterization of High Temperature Polymer Thin Films for Power Conditioning Capacitors*, Army Research Laboratory, Adelphi, MD, 2009.

25. X. Chen, E. Allahyarov, D. Langhe, M. Ponting, D. E. Schuele, E. Baer and L. Zhu, *Compos. B Eng.*, 2020, revison submitted.

26. H. Huang, X. Chen, K. Yin, I. Treufeld, D. E. Schuele, M. Ponting, D. Langhe, E. Baer and L. Zhu, *ACS Appl. Energy Mater.*, 2018, **1**, 775-782.

27. Z. Li, X. Chen, C. Zhang, E. Baer, D. Langhe, M. Ponting, M. Brubaker, T. Hosking, R. Li, M. Fukuto and L. Zhu, *ACS Appl. Polym. Mater.*, 2019, **1**, 867-875.

28. H. Huang, X. Chen, R. Li, M. Fukuto, D. E. Schuele, M. Ponting, D. Langhe, E. Baer and L. Zhu, *Macromolecules*, 2018, **51**, 5019-5026.

29. L. Yang, J. Ho, E. Allahyarov, R. Mu and L. Zhu, *ACS. Appl. Mater. Interfaces*, 2015, **7**, 19894-19905.

30. K. Yin, J. Zhang, Z. Li, J. Feng, C. Zhang, X. Chen, A. Olah, D. E. Schuele, L. Zhu and E. Baer, *J. Appl. Polym. Sci.*, 2019, **136**, 47535.

31. Z. Zhang, M. H. Litt and L. Zhu, *Macromolecules*, 2018, **51**, 1967-1977.

32. T. Yoshio, T. Yoshio, K. Ko, F. Ryoichi, Y. Masakuni, T. Waichiro and O. Shigeru, *Bull. Chem. Soc. Jpn.*, 1969, **42**, 1878-1881.

33. I. Hernandezfuentes, F. Reystolle, L. H. Tagle and E. Saiz, *Macromolecules*, 1992, **25**, 3291-3292.

34. E. Saiz, C. Abradelo, J. Mogin, L. H. Tagle and I. Hernandezfuentes, *Macromolecules*, 1991, **24**, 5594-5598.

35. L. C. E. Struik, *Physical Aging in Amorphous Polymers and Other Materials*, Elsevier Scientific Pub. Co., Amsterdam, 1978.

36. J. M. Hutchinson, *Prog. Polym. Sci.*, 1995, **20**, 703-760.

37. S. Havriliak and S. Negami, *Polymer*, 1967, **8**, 161-210.

38. A. Sawada, K. Tarumi and S. Naemura, *Jpn. J. Appl. Phys.*, 1999, **38**, 1418-1422.

39. A. Sawada, *J. Chem. Phys.*, 2008, **129**, 064701.

40. R. Coelho, *Physics of Dielectrics for the Engineer*, Elsevier Scientific Pub. Co., Amsterdam, 1979.

41. M. Dressel and M. Scheffler, *Ann. Phys.*, 2006, **15**, 535-544.

42. K. A. Verkhovskaya, A. C. Saidov and A. V. Vannikov, *Proc. SPIE, Xerographic Photoreceptors and Organic Photorefractive Materials IV*, 1998, **3471**, 117-120.

TABLE OF CONTENT GRAPHIC

AUTHOR NAMES

Xinyue Chen, Elshad Allahyarov,* Deepak Langhe, Michael Ponting, Donald E. Schuele, Eric Baer, and Lei Zhu*

TITLE

Reducing dielectric loss and enhancing electrical insulation for multilayer polymer films by nanoconfined ion transport under high poling electric fields

TEXT

High-field electric poling lock impurity ions at interfaces in multilayer polymer films, which enhance dielectric insulation and reduce ionic conduction loss for electric energy storage applications.

GRAPHICAL ABSTRACT FIGURE